

# Numerical modelling of seismic waves scattered by hydrofractures: application of the indirect boundary element method

Tim Pointer,<sup>1,\*</sup> Enru Liu<sup>1</sup> and John A. Hudson<sup>2</sup>

<sup>1</sup> Global Seismology and Geomagnetism Group, British Geological Survey, West Mains Road, Edinburgh, EH9 3LA, UK

<sup>2</sup> Department of Applied Mathematics and Theoretical Physics, University of Cambridge, Silver Street, Cambridge, CB3 9EW, UK

Accepted 1998 June 1. Received 1998 May 18; in original form 1998 February 5

## SUMMARY

We use a numerical method that can model the seismic waveforms scattered from an arbitrary number of fractures that are either empty, or contain elastic or fluid material. The indirect boundary element method (BEM) is capable of generating the full elastic wavefield and is programmed in two dimensions. The governing equations and discrete implementation of the technique are described. We explain in detail a new approach for evaluating the improper boundary integrals.

The method is shown to be highly accurate from a comparison with mode summation. Subsequently, the BEM is applied to modelling hydrofractures. Synthetic examples, calculated for cross-well and single-well geometries, demonstrate the effects of crack length, opening and infill on recorded displacements. It is shown that diffractions from the tips can, in principle, be used to locate and determine the hydrofracture size. These arrivals depart from ray theoretical traveltimes due to defocusing over a Fresnel zone. *S*-wave diffractions generally have a larger amplitude than the diffracted *P* waves, and so may provide a better indication of fracture size. Energy that is converted to interface waves and subsequently diffracted from the crack tips is also observed. The presence of water allows energy to pass through the fracture; this is clearly evident on the cross-well seismograms. Closure of the fracture causes a further increase in transmission amplitude as less energy is attenuated through internal multiples.

**Key words:** boundary element method, crack tip diffraction, hydrofracture, improper integral, interface waves.

## 1 INTRODUCTION

The motivation for analysing time-dependent seismic data is to understand how temporal changes in the elastic wavefield can be generated by external influences such as those that occur during improved oil recovery (IOR). Modelling the seismic response produced during a hydraulic fracturing treatment is of particular interest: hydrofracturing is the primary means of increasing the hydrocarbon production from a well (Vinegar *et al.* 1992). Ideally, if it were possible to determine the location, dimensions and infill of the hydrofracture throughout the treatment then the efficacy of the production programme could be optimized accordingly.

The modelling of seismic waves scattered by cracks or fractures has taken a variety of approaches. Analytical solutions for the diffracted seismic wavefield produced by

a fracture are only available for single cracks with a simple geometry (Mal 1970), and in some cases are only valid in the far field (Liu, Crampin & Hudson 1997). Seismologists have to employ numerical approaches in order to simulate the diffracted wavefield produced by models that approach anything like the real scenario.

Each method has inherent advantages and disadvantages. In some techniques simplifications or approximations to the representation of the elastic wavefield are invoked to reduce memory requirements and computation time so that complex models can be considered. Other methods can synthesize the full wavefield but the investigator is limited to using a much simpler parametrization. With the advent of powerful parallel computers more researchers are starting to adopt the latter approach. The techniques employed so far to study seismic wave scattering problems include Maslov theory (Chapman & Drummond 1982), the finite difference method (Fehler & Aki 1978), the finite element method (Lysmer & Drake 1972), the Born approximation (Wu & Aki 1985), the complex-screen approach (Wu 1994), Kirchhoff–Helmholtz integration

\*Now at: BG Technology, Gas Research and Technology Centre, Ashby Road, Loughborough, Leicestershire, LE11 3GR, UK. E-mail: timp@bgtech.co.uk

(Neuberg & Pointer 1995), the boundary integral equation method (Benites, Aki & Yomogida 1992) and the boundary element method (BEM) (Chen & Zhou 1994).

An indirect BEM is used in this paper. The main advantage is that an integral representation of the elastic wavefield allows one to model fractures with an arbitrary shape. The complete wavefield is produced, including all multiples and reverberations, and in fact the only approximation involved is the discretization of the crack surface into a number of linear elements. To keep computation times to within reasonable limits, the implementation is in two dimensions, and therefore the analysis is restricted to modelling the cross-section of a hydrofracture.

In the following section the governing equations and implementation of the BEM are examined, and the advantages and disadvantages of using this approach are made apparent. A comparison is made with analytical solutions. This is followed by synthetic examples that show the effects on the diffracted radiation pattern of different crack geometries and infills. Salient features that may be evident in field data are examined. This leads on to a final discussion and some remarks.

## 2 GOVERNING EQUATIONS AND DISCRETE IMPLEMENTATION

The BEM approach to solving physical problems is based upon formulating the governing expressions in terms of boundary integral equations. The derivation of the background theory has been carried out in similar forms by Banerjee & Butterfield (1981), Bonnet (1989), Coutant (1989) and Sánchez-Sesma & Campillo (1991), and is explained clearly in Appendix A.

### Elastic inclusions

Consider an exterior unbounded (E) region,  $D^E$ , within which there is a source of elastic radiation, and an interior (I) region,  $D^I$ , surrounded by a surface  $S$  (Fig. 1). The total displacement wavefield  $\mathbf{u}^{(t)}$  in the exterior region at a point  $\mathbf{x}$  consists of two parts: (i) a known incident wave  $\mathbf{u}^{(i)}$  due to the source alone, and (ii) a diffracted wave  $\mathbf{u}^{(d)}$ ; it can be expressed as

$$u_j^{(t)}(\mathbf{x}) = u_j^{(i)}(\mathbf{x}) + u_j^{(d)}(\mathbf{x}). \quad (1)$$

The total wavefield in the interior region comprises the refracted displacements

$$u_j^{(t)}(\mathbf{x}) = u_j^{(r)}(\mathbf{x}). \quad (2)$$

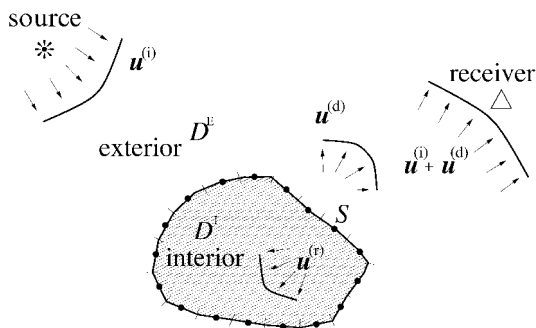


**Figure 1.** Problem configuration for the indirect BEM. The total wavefield  $\mathbf{u}^{(t)}$  in the exterior region  $D^E$  is the sum of the incident wavefield  $\mathbf{u}^{(i)}$  generated by the source and the scattered wavefield  $\mathbf{u}^{(d)}$ .

Similar expressions can be written for the tractions both inside and outside the inclusions.

The boundary conditions on  $S$  are the continuity of displacement and traction. Therefore, we can equate (1) and (2) and the corresponding expressions for the tractions at all points of  $S$  as expressed by eqs (A13). We now substitute discrete versions of eqs. (A8), (A9) and (A12) for the diffracted and refracted displacements and tractions and obtain the following:

$$\sum_{l=1}^M \bar{G}_{jk}^E(\mathbf{x}_m, \xi_l) \phi_{kl}^E - \sum_{l=1}^M \bar{G}_{jk}^I(\mathbf{x}_m, \xi_l) \phi_{kl}^I = -u_j^{(i)}(\mathbf{x}_m), \quad m=1, M, \quad (3)$$

$$\sum_{l=1}^M \bar{T}_{jk}^E(\mathbf{x}_m, \xi_l) \phi_{kl}^E - \sum_{l=1}^M \bar{T}_{jk}^I(\mathbf{x}_m, \xi_l) \phi_{kl}^I = -t_j^{(i)}(\mathbf{x}_m), \quad m=1, M.$$

To achieve this, the surface  $S$  has been discretized into  $M$  linear elements of size  $\Delta S_l$  ( $l=1, 2, \dots, M$ ). Expression (3) represents a system of linear equations for the unknown quantities  $\phi_{kl}^E = \phi_k^E(\xi_l) \Delta S_l$  and  $\phi_{kl}^I = \phi_k^I(\xi_l) \Delta S_l$  ( $l=1, 2, \dots, M$ ). On the right-hand side are the incident displacements  $\mathbf{u}^{(i)}$  and tractions  $\mathbf{t}^{(i)}$  at the midpoints  $\mathbf{x}_m$  of the surface elements on the boundary  $S$  (Fig. 1). The incident wavefield is that which would exist in the absence of any scattering surfaces, and can be calculated analytically using for example an expression for a plane wave propagating from infinity or a moment tensor description of a point source.

The kernels in (3) consist of (i)  $\bar{G}_{jk}^E(\mathbf{x}_m, \xi_l)$  and  $\bar{G}_{jk}^I(\mathbf{x}_m, \xi_l)$ , the displacement Green's functions for the  $l$ th element corresponding to the exterior and interior regions, respectively, and (ii)  $\bar{T}_{jk}^E(\mathbf{x}_m, \xi_l)$  and  $\bar{T}_{jk}^I(\mathbf{x}_m, \xi_l)$ , the traction Green's tensors for the  $l$ th element. They can be calculated using

$$\bar{G}_{jk}(\mathbf{x}_m, \xi_l) = \int_{\Delta S_l} G_{jk}(\mathbf{x}_m, \xi) dS_\xi \quad (4)$$

and

$$\bar{T}_{jk}(\mathbf{x}_m, \xi_l) = \pm \frac{1}{2} \delta_{jk} \delta_{ml} + \int_{\Delta S_l} T_{jk}(\mathbf{x}_m, \xi) dS_\xi, \quad (5)$$

where  $G_{jk}$  and  $T_{jk}$  are, respectively, the displacement and traction Green's functions, and the  $+/ -$  signs correspond to the interior and exterior regions respectively. Our implementation is in 2-D isotropic media, so  $P$ - $SV$  and  $SH$  motions are decoupled. The full-space Green's functions are employed and are given in Appendix B. They can also be calculated numerically using the discrete wavenumber method (Bouchon 1987). The simultaneous equations (3) are valid for three dimensions (Sánchez-Sesma & Luzón 1995) and full anisotropy (Wang, Achenbach & Hirose 1996) providing  $\bar{G}_{jk}$  and  $\bar{T}_{jk}$  can be evaluated.

Integrals (4) and (5) can be calculated by numerical means, such as Gaussian quadrature (Press *et al.* 1992). There is a singularity in both the displacement and the traction Green's functions where the load point  $\xi_l$  coincides with the field point  $\mathbf{x}_m$  (Appendix C). Closed-form solutions for the displacement integration in two dimensions have been given recently by Tadeu, Kausel & Vrettos (1996). The singularity in displacement is logarithmic (see eq. C2) and therefore weak, so we simply integrate as usual over the element with midpoint  $\xi_l$  in

our code. However, the singularity in traction is of the form  $1/r$  (see eq. C4), where  $r = |\mathbf{x}_m - \xi_l|$ , and cannot be integrated over. Integral (5) is, therefore, improper (Appendix C) and must be understood as a Cauchy Principal Value integral, whereby the second term on the right-hand side is null if  $m=l$ , as the limiting form is an odd function. The preceding double Dirac delta term is positive for the interior region, as  $\mathbf{x}_m$  approaches  $\xi_l$  from the inside of  $S$ , and negative for the exterior region, as  $\mathbf{x}_m$  approaches  $\xi_l$  from the outside of  $S$ .

The simultaneous linear equations (3) are solved for  $\phi_{jk}^E$  and  $\phi_{jk}^I$ , the two fictitious source distributions corresponding to the exterior and interior regions of the surface  $S$ , respectively. The final step is to calculate the refracted displacement  $\mathbf{u}^{(r)}$  inside an inclusion or the diffracted displacement  $\mathbf{u}^{(d)}$  in the exterior region at an arbitrary point  $\mathbf{x}$  using the discrete versions of eq. (A8):

$$u_j^{(r)}(\mathbf{x}) = \sum_{l=1}^M \bar{G}_{jk}^I(\mathbf{x}, \xi_l) \phi_{kl}^I \quad (6)$$

and eq. (A11):

$$u_j^{(d)}(\mathbf{x}) = \sum_{l=1}^M \bar{G}_{jk}^E(\mathbf{x}, \xi_l) \phi_{kl}^E. \quad (7)$$

It should be noted that eq. (3) is valid for any number of arbitrarily shaped cracks each possibly enclosing a different elastic material: the kernels  $\bar{G}_{jk}^I$  and  $\bar{T}_{jk}^I$  simply have to be calculated using the appropriate elastic parameters corresponding to the interior material at each element with midpoint  $\xi_l$ . The matrix sizes for  $SH$  and  $P-SV$  problems concerning elastic inclusions in two dimension are  $(2M \times 2M)$  and  $(4M \times 4M)$ , respectively.

### Cavities

If all the inclusions or fractures are gas filled (effectively dry) then the only boundary condition is that of a traction-free boundary, and eqs (3) reduce to

$$\sum_{l=1}^M \bar{T}_{jk}^E(\mathbf{x}_m, \xi_l) \phi_{kl}^E = -t_j^{(i)}(\mathbf{x}_m), \quad m=1, M. \quad (8)$$

The matrix sizes are now  $(M \times M)$  and  $(2M \times 2M)$  for  $SH$  and  $P-SV$  problems, respectively.

### Fluid inclusions

In the case of fluid-filled inclusions the same boundary conditions as a cavity apply for  $SH$  waves, and once again there is an  $M \times M$  system of equations to be solved. However, for  $P-SV$  the boundary conditions are the continuity of normal stresses and normal displacements, and the annulment of shear stresses within the fluid. In this case the equations are constructed in a local coordinate system corresponding to the normal (suffix  $n$ ) and tangential (suffix  $s$ ) directions at each field point  $\mathbf{x}_m$ , resulting in a size reduction to  $3M \times 3M$  (Coutant 1989; Dong, Bouchon & Toksöz 1995) to give the

discrete version of eqs (A19):

$$\begin{aligned} \sum_{l=1}^M \bar{G}_{nk}^E(\mathbf{x}_m, \xi_l) \phi_{kl}^E - \sum_{l=1}^M \bar{G}^I(\mathbf{x}_m, \xi_l) \phi_l^I &= -u_n^{(i)}(\mathbf{x}_m), \quad m=1, M, \\ \sum_{l=1}^M \bar{T}_{nk}^E(\mathbf{x}_m, \xi_l) \phi_{kl}^E - \sum_{l=1}^M \bar{T}^I(\mathbf{x}_m, \xi_l) \phi_l^I &= -t_n^{(i)}(\mathbf{x}_m), \quad m=1, M, \\ \sum_{l=1}^M \bar{T}_{sk}^E(\mathbf{x}_m, \xi_l) \phi_{kl}^E &= -t_s^{(i)}(\mathbf{x}_m), \quad m=1, M. \end{aligned} \quad (9)$$

In this case the unknown fictitious line forces are  $\phi_{kl}^I = \phi_k^E(\xi_l) \Delta S_l$  and  $\phi_l^I = \phi^I(\xi_l) \Delta S_l$  ( $l=1, 2, \dots, M$ ).  $\bar{G}_{nk}^E$ ,  $\bar{T}_{nk}^E$  and  $\bar{T}_{sk}^E$  are the line element Green's functions as before (eqs 4 and 5).  $\bar{G}^I$  and  $\bar{T}^I$  are the corresponding quantities for the fluid, with

$$\bar{G}^I(\mathbf{x}_m, \xi_l) = \frac{1}{2} \delta_{ml} + \int_{\Delta S_l} G^I(\mathbf{x}_m, \xi) dS_\xi \quad (10)$$

and

$$\bar{T}^I(\mathbf{x}_m, \xi_l) = -\rho \omega^2 \int_{\Delta S_l} T^I(\mathbf{x}_m, \xi) dS_\xi, \quad (11)$$

where  $\rho$  is the fluid density and  $\omega$  is the angular frequency.

It is not possible to model liquid inclusions by substituting a small value for the interior  $S$ -wave speed into eq. (3). The matrix on the left-hand side becomes ill-conditioned and the numerical solution unstable.

One can assign  $N$  elements for the interior surface and  $M$  elements for the exterior surface in the case of a solid or fluid-filled inclusion. This leads to a  $(2M+2N) \times (2M+2N)$  matrix system for the case of  $P-SV$  waves interacting with a solid scatterer. If the wave speeds in the interior are much different from those in the exterior then a considerable amount of computer time and memory can be saved. However, the approach to element integrations of tractions over the boundary has to be modified.

It is straightforward to model any combination of cavities, and elastic and fluid inclusions. The single scattering or Born approximation can be evaluated by making all the matrix terms that describe crack-crack interactions in eqs (3), (8) or (9) equal to zero. It is possible to include a free surface (Yokoi & Sánchez-Sesma 1998) or to place the inhomogeneities within a layer by introducing extra elements. We do not consider a solid-filled fracture, which could be used to model fault gouge. In the numerical experiments in Section 4 we examine only dry and water-filled fractures situated in an unbounded space.

### 3 TEST OF ACCURACY

It is necessary to check the output of any waveform modelling code with analytical solutions or to compare it with other methods whose results are known to be exact. This is especially important if synthetic data are to be subsequently compared with observed seismograms. We computed the scattered radiation pattern produced when a plane wave impinges on a cylindrical inclusion or cavity of radius  $a$  using the method of wave-functions expansion (Pao & Mow 1973), whereby the scattered wavefield is expressed as a superposition of a series of outgoing cylindrical standing-wave modes. The modulus of

the diffracted displacement field is calculated at 100 receiver points equally spaced on a circumference equal to  $10a$ , where  $a$  is the radius of the scatterer, in a similar manner to Benites *et al.* (1992). The calculations are performed for an  $SH$  wave incident on a cavity and a hard elastic inclusion, and for a  $P$  wave interacting with a cavity, fluid-filled inclusion and soft elastic inclusion, respectively (Tables 1 and 2), in each case for values of  $k_\beta a$  equal to  $2\pi$  and  $8\pi$ , where  $k_\beta$  is the angular  $S$ -wavenumber for the exterior region. For each BEM calculation the inhomogeneity surface was discretised into 400 elements giving 16 elements per  $S$  wavelength in the case  $k_\beta a = 8\pi$ . The results for  $SH$  and  $P$ - $SV$  are displayed in Figs 2 and 3, respectively.

**Table 1.** The dimensionless  $S$ -wave speeds ( $\beta$ ) and densities ( $\rho$ ) used for calculating the  $SH$  radiation patterns shown in Fig. 2.

	exterior	interior
cavity	$\beta = 1.0$ $\rho = 1.0$	
hard elastic inclusion	$\beta = 1.0$ $\rho = 1.0$	$\beta = 1.6$ $\rho = 1.3$

**Table 2.** The dimensionless  $P$ -wave speeds ( $\alpha$ ),  $S$ -wave speeds ( $\beta$ ) and densities ( $\rho$ ) used for calculating the  $P$ - $SV$  radiation patterns shown in Fig. 3.

	exterior	interior
cavity	$\alpha = 1.73$ $\beta = 1.0$ $\rho = 1.0$	
liquid inclusion	$\alpha = 1.73$ $\beta = 1.0$ $\rho = 1.0$	$\alpha = 1.0$ $\rho = 0.8$
soft elastic inclusion	$\alpha = 1.73$ $\beta = 1.0$ $\rho = 1.0$	$\alpha = 1.0$ $\beta = 0.7$ $\rho = 0.8$

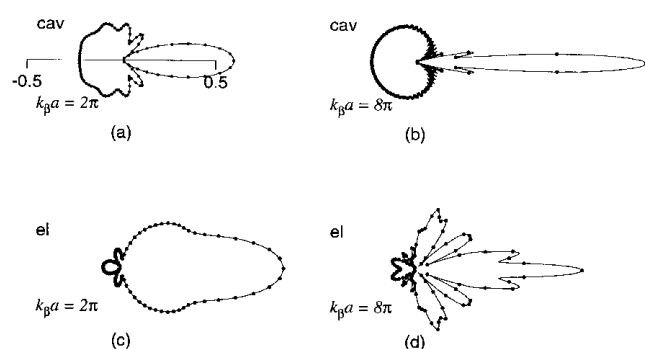


**Figure 2.** The scattered radiation pattern for  $SH$  (Table 1). The modulus of the pure diffracted field is plotted for the cases of a plane wave impinging upon (i) a cavity (cav) in (a) and (b), and (ii) an elastic (el) inclusion in (c) and (d), and in each case for values of  $k_\beta a = 2\pi$  and  $8\pi$ , respectively, where  $k_\beta$  is the angular  $S$  wavenumber and  $a$  is the radius. The solid lines are the numerical results produced using the BEM and the solid circles are the analytical solutions computed using mode summation (Pao & Mow 1973).

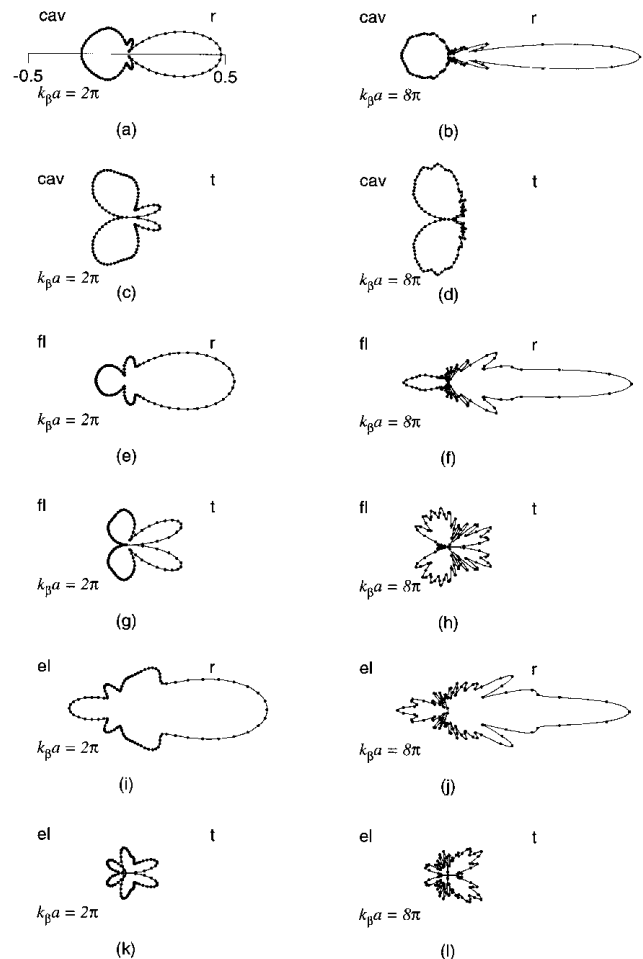


**Figure 3.** The scattered radiation pattern for  $P$ - $SV$  (Table 2). The modulus of the pure diffracted field is plotted for the cases of a plane  $P$  wave impinging upon (i) a cavity (cav) in (a)–(d), (ii) a fluid (fl) inclusion in (e)–(h), and (iii) an elastic (el) inclusion in (i)–(l). In each case the calculations were performed for values of  $k_\beta a = 2\pi$  and  $8\pi$ , respectively, where  $k_\beta$  is the angular  $S$  wavenumber corresponding to the exterior region and  $a$  is the radius. The radial and tangential values are denoted  $r$  and  $t$ , respectively. The solid lines are the numerical results produced using the BEM and the solid circles are the analytical solutions computed using mode summation (Pao & Mow 1971).

The results show an excellent agreement between the BEM synthetic (solid lines) and mode-summation (solid circles) results. The accuracy is obviously dependent on the number of elements used to prescribe the boundary: a finer discretization is needed to produce the same accuracy at a higher frequency. A further check could be carried out to determine the residual tractions along the boundary (Benites *et al.* 1992).

When parts of the surface are separated by only a very small distance eqs (3), (8) and (9) become nearly degenerate. This leads to ill-conditioning of the algebraic equations (Krishnasamy, Rizzo & Liu 1994). However, from numerical tests we found that the BEM code is accurate when modelling the thin cracks used in the following section. A further suitable check would be to compare with Mal's crack (Bouchon 1987).

#### 4 SCATTERING BY A HYDROFRACTURE

The BEM code was used to model the seismic wavefield diffracted by a single hydrofracture. The influence of different crack parameters on the scattered displacements was assessed. In particular, we wanted to see the effects of fracture length, fracture opening and fracture infill, and observe the differences between the forward- and backscattered wavefields.

The model geometry used to generate the synthetic seismograms is shown in Fig. 4. The source, receivers and hydrofracture are situated in an elastic ( $\alpha_c = 3500 \text{ m s}^{-1}$ ,  $\beta_c = 2023 \text{ m s}^{-1}$ ,  $\rho_c = 2300 \text{ kg m}^{-3}$ ) full space. In all the examples, we used a dilatational line source situated at the origin. For the cross-well geometry there are 51 receivers equally spaced between (200 m, -200 m) and (200 m, 200 m), and to represent a single well set-up the sensors are placed between (0, -200 m) and (0, 200 m) (Fig. 4). The centre line of the fracture lies between (100 m,  $-h/2$ ) and (100 m,  $h/2$ ), where  $h$  is the length of the crack.

The source signal is a Ricker wavelet (Ricker 1977) with a peak frequency of 100 Hz. Seismograms were calculated using 128 discrete frequencies and a Nyquist value equal to 800 Hz. Both the  $x$ - and  $z$ -components of displacement are plotted for each model. The total displacement is displayed in the case of a cross-well geometry and the pure scattered field for the

single-well set-up. The same scale is used for all the traces and in each plot.

The hydrofracture is modelled as a single crack represented by a thin rectangle. In reality a fracture would be highly irregular with many asperities and contact points; however, we assume that its average seismic properties can be approximated with a thin planar layer (Liu *et al.* 1995). Each corner node is replaced with two nodes that are placed 0.05 times the local element length away from the corner, in order to treat the problem of the singularity in traction (Banerjee & Butterfield 1981). We used an element length equal to 1 m, which gave 20 elements per dominant  $S$  wavelength. For each set of seismograms the fracture infill, length and thickness, together with the field geometry (cross-well or single well) are displayed above the traces. The various arrivals on each synthetic seismogram can be compared with the ray theoretical times displayed in Fig. 5, which all have the fracture length and field geometry shown.

#### Fracture infill

The suite of seismograms shown in Fig. 6 correspond to a model of a fracture that is 200 m in length and 1 m in thickness, with the source and receivers placed in a cross-well geometry. The top traces relate to a dry fracture and the lower ones to a

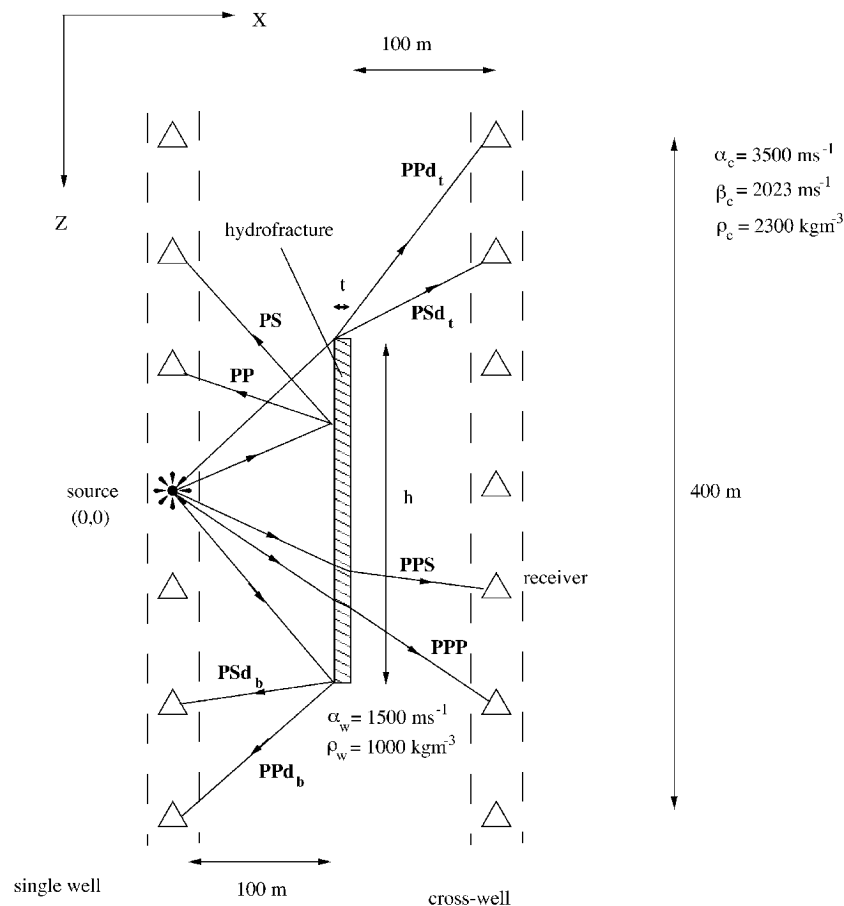


**Figure 4.** Cross-well and single-well geometries for calculating BEM synthetics. The source, receivers and fracture are situated in a full space. The ray paths of the  $P$  waves generated by the explosive line source that interact with the crack are shown schematically.  $PP$  and  $PS$  are  $P$  and  $S$  waves reflected at the crack boundary. The crack-tip  $P$ -wave diffractions are denoted  $PPd_t$  and  $PPd_b$ , where the subscripts  $t$  and  $b$  indicate whether the energy was diffracted at the 'top' or 'bottom' of the fracture, respectively. Similarly, the  $P$ -to- $S$  converted waves that are diffracted are called  $PSd_t$  and  $PSd_b$ .

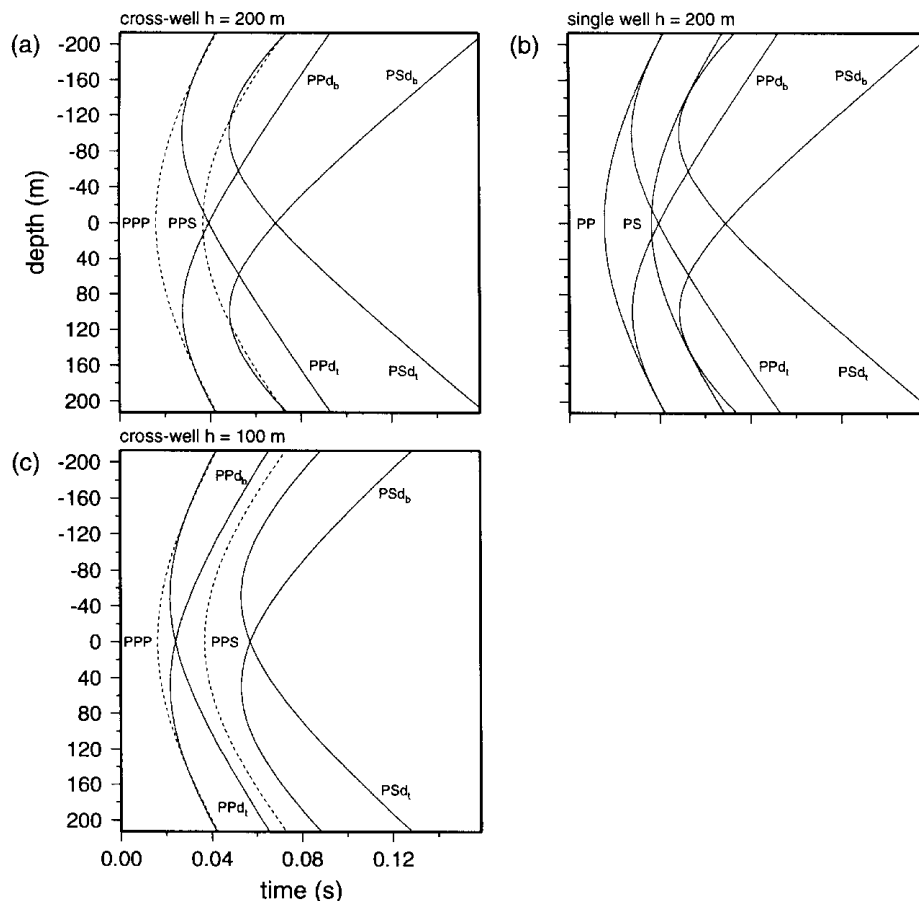


**Figure 5.** Ray-theoretical traveltimes (with respect to the centre of the incident pulse) for diffracted, reflected and transmitted waves (dashed). The labels are explained in Fig. 4. The traveltimes according to the models used to generate the seismograms in Figs 6, 8(a) and 8(c) (the change in traveltime due to the reduced crack opening is negligible) are shown in (a). The times in (b) correspond to the single-well geometry needed to produce Fig. 7. The graph in (c) corresponds to Fig. 8(b)

water ( $\alpha_w = 1500 \text{ m s}^{-1}$ ,  $\rho_w = 1000 \text{ kg m}^{-3}$ ) filled one. It is possible to observe diffractions from the crack tips: there are  $P$ -wave diffractions from the top ( $PPd_t$ ) and bottom ( $PPd_b$ ) of the crack (more clearly seen on the  $x$ -component). Similarly, there is energy that is converted from  $P$  to  $S$  that is diffracted from the ends of the fracture ( $PSd_t$  and  $PSd_b$ ) (more evident on the  $z$ -component). The minimum points in the traveltime curves of the diffracted waves clearly define the vertical extent of the fracture (Fig. 5). The fracture causes a shadow zone in the direct  $P$  arrivals. This is more apparent in the dry case as no energy passes through. Acoustic waves that travel through the fluid-filled crack can re-emerge as a  $P$  ( $PPP$ ) or  $S$  wave ( $PPS$ ). There seems to be a precursor to the  $PSd$  arrivals for the dry fracture (noticeable on the  $z$ -component between stations 40 and 80 m, and  $-80$  and  $-40$  m in Fig. 6(a) and marked with the label A). This is simply the effect of defocusing over the Fresnel zone: the wavelet extends in time and decreases in amplitude. In general the  $PSd$  arrivals are larger than the  $PPd$  ones and therefore might be more observable in real data. However, it is likely that they are much more strongly attenuated due to intrinsic absorption.

The boundary element program generates the full wavefield including all the interface waves and all internal multiples that constitute waveguides. The inhomogeneous waves produced at the crack boundary are not detectable in our synthetics due

to exponential decay of amplitude with distance. However, their subsequent conversions to body waves are visible. If the scaling was changed in the seismograms to boost the low amplitudes one would observe two types of converted interface waves: (i)  $P$  waves that arrive at the centre of the hydrofracture, convert to Rayleigh (dry cracks) or Stoneley waves (fluid-filled cracks), and are diffracted from the crack tips as either  $P$  waves or  $S$  waves; and (ii)  $P$  waves that arrive at the ends of the hydrofracture, convert to an interface wave, travel to the opposite tip and are finally diffracted. An example of the former type, which converts to a Stoneley wave at the crack centre and is diffracted as a  $P$  wave, is shown in Fig. 6(b) (label B).

The models used to produce the traces in Fig. 7 are identical to those used for Fig. 6 except that the source and receivers are now placed in a single-well geometry (Fig. 4). Only the pure scattered field is shown. It is now possible to see the effect of the presence of a hydrofracture on the backscattered energy. The reflected ( $PP$ ) and converted ( $PS$ ) phases are easy to observe in addition to the crack tip diffractions. As expected the reflected and diffracted amplitudes are larger in the case of a cavity as some energy can travel through the fluid-filled fracture. However, the difference in wavefields caused by the different infill does not manifest itself so clearly as in the case of the cross-well geometry.

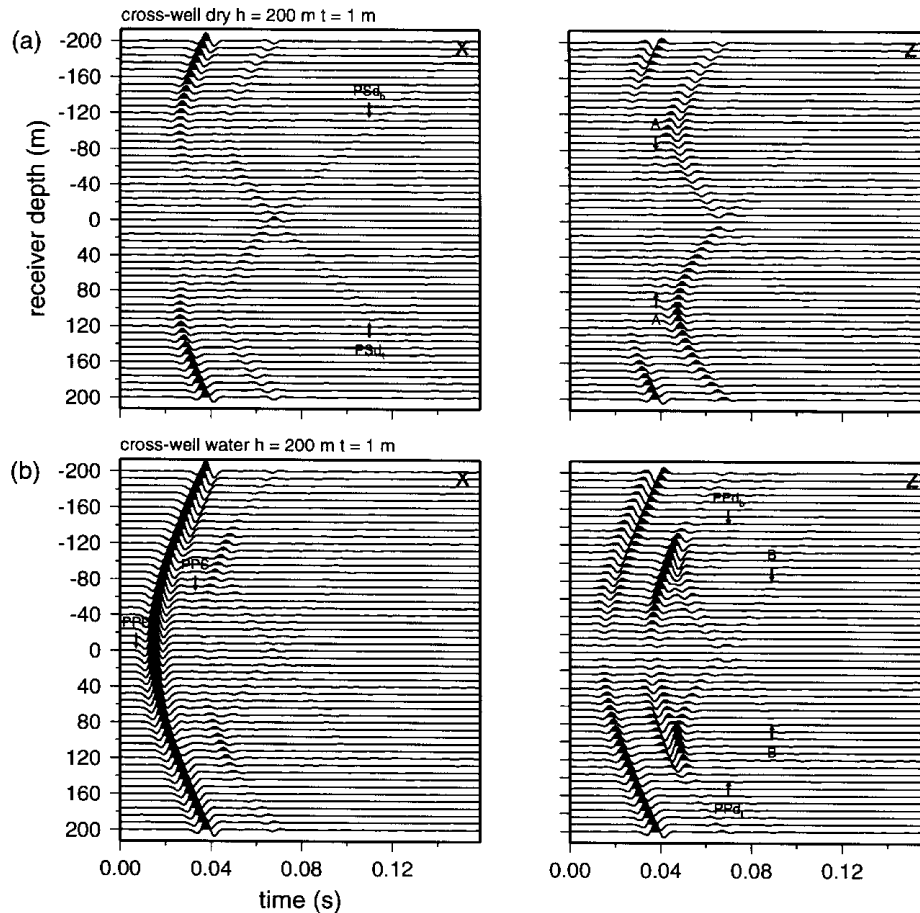


**Figure 6.** BEM synthetic horizontal- (x) and vertical- (z) component seismograms for the cross-well geometry depicted in Fig. 4. The total wavefield is plotted. The fracture length is 200 m and the fracture opening is 1 m. The traces shown in (a) and (b) correspond to a dry and a water-filled fracture, respectively. The energy marked with the label A occurs due to defocusing at the crack tips. The arrival labelled B is a *P* wave that arrives at the crack centre, travels along the crack surface as a Stoneley wave and is diffracted at both tips as a *P* wave.

### Fracture length

A cross-well shot gather is shown in Fig. 8(b) for a water-filled fracture whose length is reduced to 100 m; it can be compared with Fig. 8(a), which is identical to Fig. 6(b). The arrival times of the crack-tip diffractions are dramatically different. The vertical extent of the fracture is still apparent from the *PSd* phases. There is much less transmitted energy in the form of *PPP* owing to the reduced size of the fracture (clearly seen on the *z*-component). The amplitude and phase of all the arrivals are clearly affected by the fracture length.

### Fracture opening

A similar shot gather is shown in Fig. 8(c) for a water-filled crack whose length remains at 200 m and crack opening is reduced to 0.1 m. The change in thickness allows more energy to pass through as *PPP* and *PPS* because less energy is attenuated through internal multiples. The crack-tip diffractions are larger because more refracted energy can re-emerge at the crack ends. The same change in crack opening for a dry crack has no visible effect on the wavefield as there is no transmitted energy and the dominant wavelength is much larger than the crack width, although the results are not shown here.

## 5 DISCUSSION

We have demonstrated that the BEM could be a useful tool for analysing the scattering of seismic waves caused by hydraulic fractures. Our implementations for cavities and elastic inclusions is the same as those of Sánchez-Sesma & Campillo (1991) and Sánchez-Sesma & Luzón (1995), respectively, and similar to that of Coutant (1989) for the case of fluid-filled scatterers, except that we use the full-space fluid Green's function. We have explained, in detail, the evaluation of the improper boundary integrals. From a comparison with analytical solutions we have proved that our code produces highly accurate results, although this may degenerate in the proximity of the crack corners.

The synthetic experiments undertaken demonstrate how *P* and *S* waves diffracted at crack tips can be used to determine the vertical extent of the fracture; this has been achieved from the analysis of real data (Liu *et al.* 1997). The converted *PSd* diffractions have a much stronger amplitude than the *PPd* events, which suggests they could be a better indicator of fracture length, with the potential to resolve smaller-wavelength features. Energy that converts to interface waves at the fracture and is subsequently diffracted from the tips may be observable in real data if a suitable gain is applied. It is straightforward to include frequency-independent

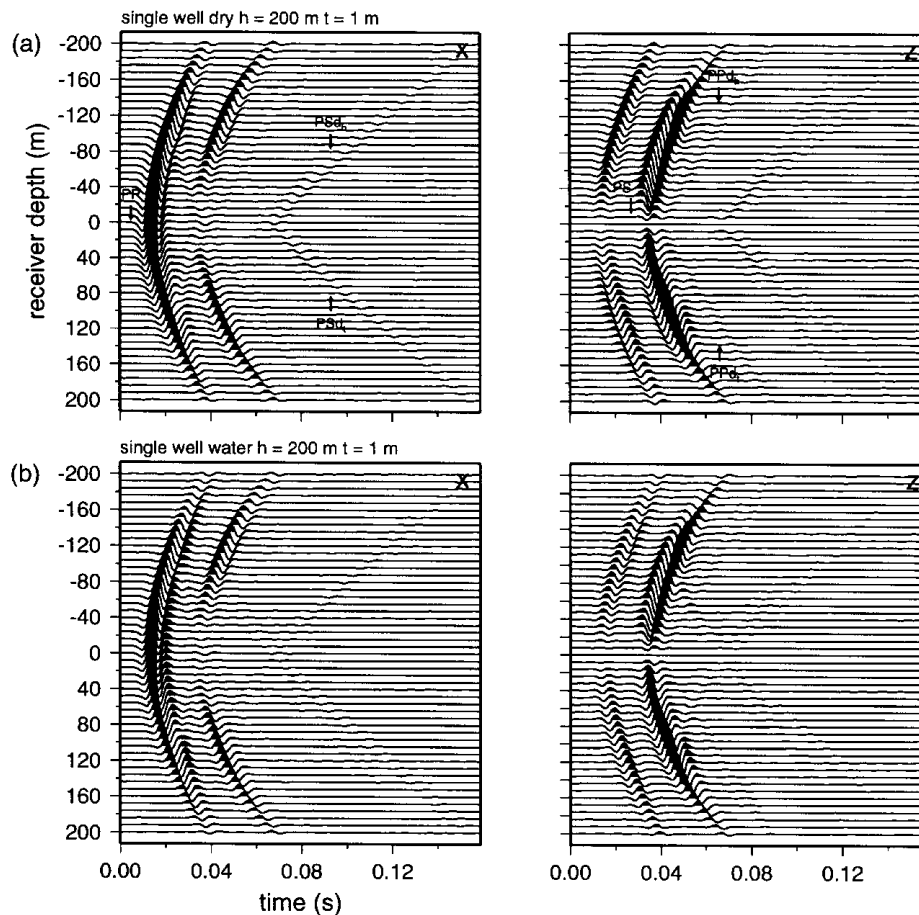


Figure 7. The same as Fig. 6 for the single-well geometry shown in Fig. 4. The pure scattered wavefield is plotted.

attenuation or viscoelasticity (Chen & Zhou 1994) in the BEM modelling; however, it is beyond the realm of this study.

The effect of a water-filled crack as opposed to an empty one is to allow acoustic energy to pass through and reduce the backscattering. The difference in the observed wavefields is more apparent for the cross-well geometry than for the single-well set-up for the models that we examine. During a hydraulic fracturing treatment there probably exists a state of partial saturation during certain periods that may give rise to high attenuation.

We show that it may be possible to detect changes in fracture dimensions through examination of the displacement wavefield. The fracture length controls the position of the minimum points on the traveltime curves. There is a strong defocusing effect of diffractions recorded at certain stations, manifesting itself in amplitude and phase variations that are affected by the fracture length. The thickness of a fluid-filled crack has a large effect on both transmitted and diffracted arrivals. Laboratory experiments performed by Groenenboom & Fokkema (1998) show that small changes in the width of a hydrofracture are directly expressed in the dispersion of the transmitted signal.

In reality the fracture would have an irregular surface, and there would exist other surrounding fractures. This gives rise to a more complex wavefield due to the effects of multiple scattering. The data analysed by Majer *et al.* (1996) are much more complicated than the synthetic examples presented here.

In order to model real data properly (Meadows & Winterstein 1994; Majer *et al.* 1996) it is necessary to incorporate the 3-D effects of the borehole source radiation pattern (Kurkjan *et al.* 1994) and to synthesize the pressure field that would be recorded inside a fluid-filled borehole (Dong & Toksöz 1995). An effective source array can be used to approximate the explicit representation of sources and receivers situated in a fluid-filled borehole. Furthermore, the hydrofracture itself should be imaged in three dimensions. Another useful extension to the modelling would be to include layering (Gerstoft & Schmidt 1991; Pedersen, Maupin & Campillo 1996; Yokoi 1996).

## ACKNOWLEDGMENTS

This paper is published by permission of the Director of the British Geological Survey (NERC) and with approval from BG plc. The first author was supported through a government funded ROPA project in conjunction with Conoco (UK) Ltd, who provided sponsorship to EL. We are indebted to the valuable advice and comparison of seismograms provided by Rafael Benites. The method in Appendix C was kindly shown to us by Paul Martin. We appreciate the discussions that took place with John Queen, Wenjie Dong and Frank Ohlsen. Comments and suggestions from David Booth, Xiang-Yang Li and the two anonymous reviewers helped to improve the manuscript.



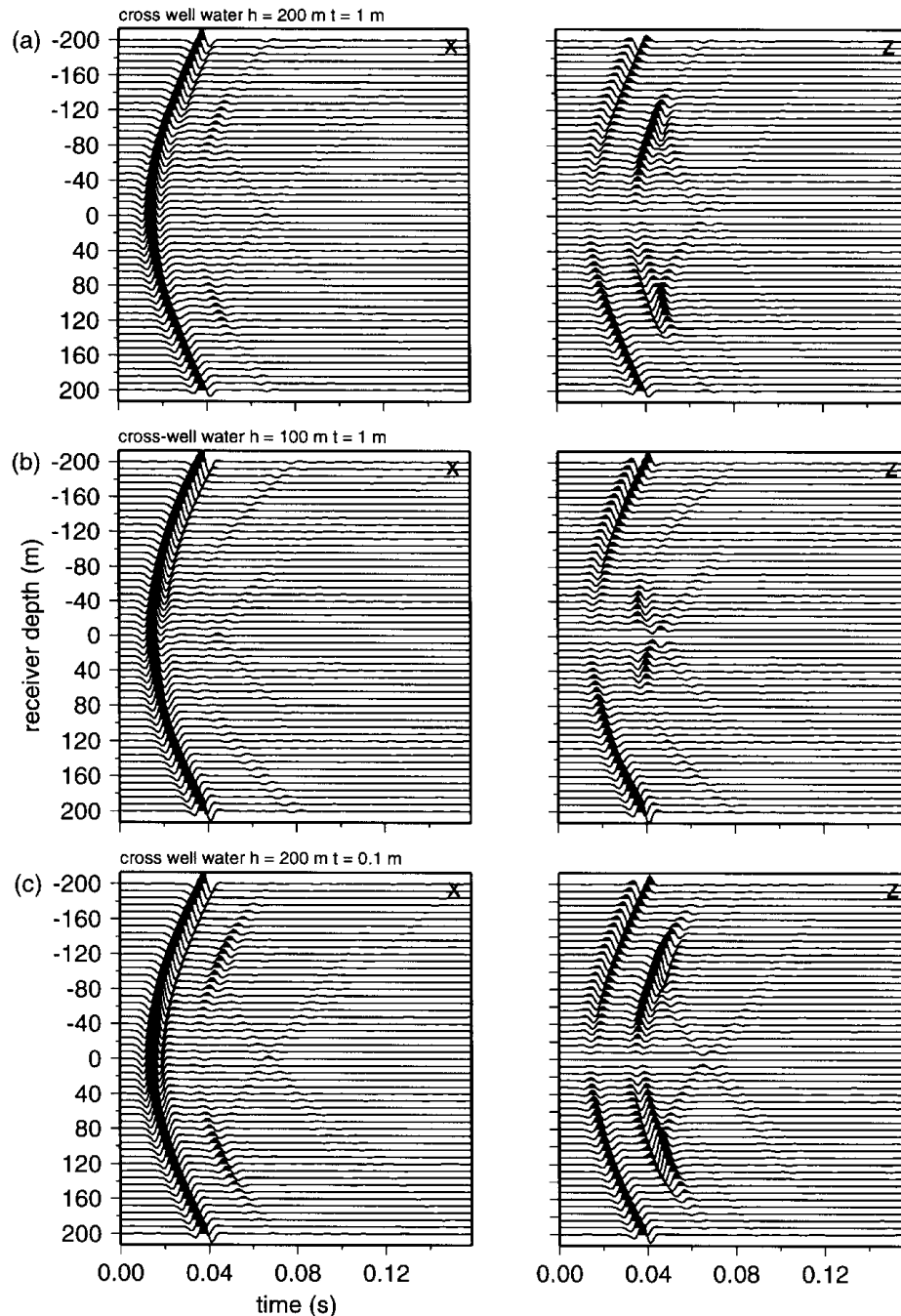


**Figure 8.** The synthetic seismograms in (a) are the same as in Fig. 6(b). The traces in (b) and (c) are also calculated using a cross-well geometry and a water-filled fracture. The fracture length in (b) is reduced to 100 m and the thickness remains at 1 m, whereas in (c) the fracture opening decreases to 0.1 m and the length is kept at 200 m. In each case the total wavefield is displayed.

## REFERENCES

- Aki, K. & Richards, P., 1980, *Quantitative Seismology: Theory and Methods*, W.H. Freeman, New York.
- Banerjee, P.K. & Butterfield, R., 1981. *Boundary Element Methods in Engineering Science*, McGraw-Hill, London.
- Benites, R., Aki, K. & Yomogida, K., 1992. Multiple scattering of SH waves in 2-D media with many cavities, *Pure appl. Geophys.*, **138**, 353–390.
- Bonnet, M., 1989. Regular boundary integral equations for three-dimensional finite or infinite bodies with and without curved cracks in elastodynamics, *Boundary Element Techniques: Applications in Engineering*, Computational Mechanics Publications, Southampton.
- Bouchon, M., 1987. Diffraction of elastic waves by cracks or cavities using the discrete wavenumber method, *J. acoust. Soc. Am.*, **81**, 1671–1676.
- Chapman, C.H. & Drummond, R., 1982. Body-wave seismograms in inhomogeneous media using Maslov asymptotic theory, *Bull. seism. Soc. Am.*, **72**, 277–317.
- Chen, G. & Zhou, H., 1994. Boundary element modelling of non-dispersive and dispersive waves, *Geophysics*, **59**, 113–118.
- Coutant, O., 1989. Numerical study of the diffraction of elastic waves by fluid-filled cracks, *J. geophys. Res.*, **94**, 17 805–17 818.
- Dominguez, J. & Abascal, R., 1984. On fundamental solutions for the boundary integral equations method in static and dynamic elasticity, *Eng. Analysis*, **1**, 128–134.

- Dong, W., 1993. Elastic wave radiation from borehole seismic sources in anisotropic media, *PhD thesis*, MIT, Cambridge, USA.
- Dong, W. & Toksöz, M.N., 1995. Borehole seismic-source radiation in layered isotropic and anisotropic media: real data analysis, *Geophysics*, **60**, 748–757.
- Dong, W., Bouchon, M. & Toksöz, M.N., 1995. Borehole seismic-source radiation in layered isotropic and anisotropic media: boundary element modelling, *Geophysics*, **60**, 735–747.
- Fehler, M. & Aki, K., 1978. Numerical study of diffraction of plane elastic waves by a finite crack with application to location of a magma lens, *Bull. seism. Soc. Am.*, **68**, 573–598.
- Gerstoft, P. & Schmidt, H., 1991. A boundary element approach to ocean seismoacoustic facet reverberation, *J. acoust. Soc. Am.*, **89**, 1629–1642.
- Graffi, D., 1946. Sul teorema di reciprocità nella dinamica dei corpo elastici, *Memorie della Accademia delle Scienze*, **4**, 103.
- Groenenboom, J. & Fokkema, J.T., 1998. Monitoring the width of hydraulic fractures with acoustic waves, *Geophysics*, **63**, 139–148.
- Kawase, H., 1988. Time-domain response of a semi-circular canyon for incident SV, P, and Rayleigh waves calculated by the discrete wavenumber boundary element method, *Bull. seism. Soc. Am.*, **78**, 1415–1437.
- Krishnasamy, G., Rizzo, F.J. & Liu, Y., 1994. Boundary integral equations for thin bodies, *Int. J. Num. Meth. Eng.*, **37**, 107–121.
- Kurkjan, A.L., Coates, R.T., White, J.E. & Schmidt, H., 1994. Finite-difference and frequency-wavenumber modelling of seismic monopole sources and receivers in fluid-filled boreholes, *Geophysics*, **59**, 1053–1064.
- Liu, E., Hudson, J.A., Crampin, S., Rizer, W.D. & Queen, J.H., 1995. Seismic properties of a general fracture, in *Proc. 2nd Int. Conference on the Mechanics of Jointed and Faulted Rock*, pp. 673–678, ed. Rossmanith, Balkema, Rotterdam.
- Liu, E., Crampin, S. & Hudson, J.A., 1997. Diffraction of seismic waves by cracks with application to hydraulic fracturing, *Geophysics*, **62**, 253–265.
- Lysmer, J. & Drake, L.A., 1972. A finite element method for seismology, *Methods of Computational Physics*, Vol. 11, Academic Press, New York.
- Majer, E.L. *et al.*, 1996. Utilising crosswell, single well and pressure transient tests for characterising fractured gas reservoirs, *Leading Edge*, **15**, 951–956.
- Mal, A.K., 1970. Interaction of elastic waves with a Griffith crack, *Int. J. Eng. Sci.*, **8**, 763–776.
- Meadows, M.A. & Winterstein, D.F., 1994. Seismic detection of a hydraulic fracture from shear-wave VSP data at Lost Hills Field, California, *Geophysics*, **57**, 11–26.
- Neuberg, J. & Pointer, T., 1995. Modelling seismic reflections from D' using the Kirchhoff method, *Phys. Earth planet. Inter.*, **90**, 273–281.
- Pao, Y.H. & Mow, C.C., 1973. *The Diffraction of Elastic Waves and Dynamic Stress Concentrations*, Crane & Russak, New York.
- Pedersen, H., Maupin, V. & Campillo, M., 1996. Wave diffraction in multilayered media with the Indirect Boundary Element Method: application to 3-D diffraction of long-period surface waves by 2-D lithospheric structures, *Geophys. J. Int.*, **125**, 545–558.
- Press, W.H., Teukolsky, S.A., Vetterling, W.T. & Flannery, B.P., 1992. *Numerical Recipes in Fortran: the Art of Scientific Computing*, 2nd edn, Cambridge University Press, Cambridge.
- Ricker, N.H., 1977. *Transient Waves in Visco-elastic Media*, Elsevier, Amsterdam.
- Ryshik, I.M. & Gradstein, I.S., 1963. *Tables of Series, Products and Integrals*, VEB Deutscher Verlag der Wissenschaften, Berlin.
- Sánchez-Sesma, F.J. & Campillo, M., 1991. Diffractions of P, SV, and Rayleigh waves by topographic features: a boundary integral formulation, *Bull. seism. Soc. Am.*, **81**, 2234–2253.
- Sánchez-Sesma, F.J. & Luzón, F., 1995. Seismic response of three-dimensional alluvial valleys for incident P, S, and Rayleigh waves, *Bull. seism. Soc. Am.*, **85**, 269–284.

- Tadeu, A.J.B., Kausel, E. & Vrettos, C., 1996. Scattering of waves by subterranean structures via the boundary element method, *Soil Dyn. Earthq. Eng.*, **15**, 387–397.
- Vinegar, H.J. *et al.*, 1992. Active and passive imaging of hydraulic fractures, *Leading Edge*, **11**, 15–22.
- Wang, C.-Y., Achenbach, J.D. & Hirose, S., 1996. Two-dimensional time domain BEM for scattering of elastic waves in solids of general anisotropy, *Int. J. Solids Structures*, **33**, 3843–3864.
- Wu, R.S., 1994. Wide-angle elastic wave one-way propagation in media with infinitely extended interfaces, *J. Phys. Earth*, **44**, 39–60.
- Wu, R.S. & Aki, K., 1985. Scattering characteristics of elastic waves by an elastic heterogeneity, *Geophysics*, **50**, 582–589.
- Yokoi, T., 1996. An indirect boundary element method based on recursive matrix operation to compute waves in irregularly stratified media with infinitely extended interfaces, *J. Phys. Earth*, **44**, 39–60.
- Yokoi, T. & Sánchez-Sesma, F.J., 1998. A hybrid calculation technique of the indirect boundary element method and the analytical solutions for three-dimensional problems of topography, *Geophys. J. Int.*, **133**, 121–139.

## APPENDIX A: 2-D BOUNDARY ELEMENT METHOD THEORY

### Elastic medium

The reciprocal theorem relates two different boundary value problems on the same region with the same boundary. It states that the work done by one set of forces  $\mathbf{f}$  and boundary tractions  $\mathbf{t}$  on the set of displacements  $\mathbf{u}^*$  in the other system is equal to the work done by the second set of forces  $\mathbf{f}^*$  and tractions  $\mathbf{t}^*$  on the first displacements  $\mathbf{u}$ . We deal with the steady-state elastodynamic problem and assume that the physical components in the representation are harmonic in time with an angular frequency  $\omega$ . The reciprocal theorem for the 2-D elastodynamic case (Graffi 1946) may be expressed as

$$\int_S t_i(\mathbf{x}, \omega) u_i^*(\mathbf{x}, \omega) ds + \int_D f_i(\mathbf{x}, \omega) u_i^*(\mathbf{x}, \omega) dA = \int_S t_i^*(\mathbf{x}, \omega) u_i(\mathbf{x}, \omega) ds + \int_D f_i^*(\mathbf{x}, \omega) u_i(\mathbf{x}, \omega) dA, \quad (\text{A1})$$

where  $S$  is the boundary to the region  $D$ . The result is a direct consequence of the symmetry in the elastic tensor,  $\{c_{ijkl} = c_{klij}\}$ , which arises from the existence of a strain-energy function.

A representation for the displacement field  $\mathbf{u}^*$  can be obtained by replacing the other displacement field  $\mathbf{u}$  with the Green's function  $G_{ij}$ , the fundamental singular solution to the elastic wave equation (Appendix B), and correspondingly the body-force term  $\mathbf{f}^*$  with a delta impulse (Aki & Richards 1980). The resulting Somigliana representation theorem expresses the displacement  $\mathbf{u}^{(r)}$  at a point  $\xi$  as an integral of the displacements and tractions over the boundary  $S$  (with respect to  $\mathbf{x}$ ), together with an integral over body forces within  $S$  (with respect to  $\mathbf{y}$ ):

$$\begin{aligned} a^1 u_j^{(r)}(\xi, \omega) &= \int_S [G_{ij}^1(\mathbf{x}, \xi, \omega) t_i^1(\mathbf{x}, \omega) - u_i^1(\mathbf{x}, \omega) c_{ipkj}^1 \hat{n}_p G_{kj,l}^1(\mathbf{x}, \xi, \omega)] ds_{\mathbf{x}} \\ &\quad + \int \int_{D^1} f_i^1(\mathbf{y}, \omega) G_{ij}^1(\mathbf{y}, \xi, \omega) dA_{\mathbf{y}}, \\ a^1 &= \begin{cases} 1 & \xi \text{ in } D^1, \\ 0 & \xi \text{ not in } D^1, \end{cases} \end{aligned} \quad (\text{A2})$$

where  $G_{ij}^I$  is the Green's function for the region  $D^I$  interior to  $S$  and  $G_{kj,l}^I(\mathbf{x}, \xi) = \partial G_{kj}^I(\mathbf{x}, \xi) / \partial x_l$ ;  $\{c_{ijpq}^I\}$  are the stiffnesses in  $D^I$ , and  $\mathbf{u}^I$  and  $\mathbf{t}^I$  are the limits of  $\mathbf{u}^{(r)}$  and  $\mathbf{t}^{(r)}$  as  $S$  is approached from the interior. The outward normal to  $S$  is given by  $\hat{\mathbf{n}}$ . To evaluate the right-hand side of eq. (A2) when  $\xi$  is situated on the boundary, we consider the limit as  $\xi$  approaches the boundary  $S$  (Appendix C), which is assumed to be smooth, from inside  $D^I$ . We can rewrite eq. (A2) as

$$a^I u_j^{(r)}(\xi) = P \int_S [G_{ij}^I(\mathbf{x}, \xi) t_i^I(\mathbf{x}) - u_i^I(\mathbf{x}) T_{ij}^I(\mathbf{x}, \xi)] ds_x + \iint_{D^I} f_i^I(\mathbf{y}) G_{ij}^I(\mathbf{y}, \xi) dA_y, \quad (\text{A3})$$

$$a^I = \begin{cases} 1 & \xi \text{ in } D^I, \\ 0 & \xi \text{ not in } D^I, \\ 0.5 & \xi \text{ on } S, \end{cases}$$

where we have substituted the expression for the traction Green's function  $T_{ij}(\mathbf{x}, \xi) = c_{ipkl} \hat{n}_p(\mathbf{x}) G_{kj,l}^I(\mathbf{x}, \xi)$ .  $P$  denotes the Cauchy Principal Value (Appendix C). Eq. (A3) is the representation used in the direct BEM. The boundary conditions on  $S$  are applied to determine the unknown boundary values  $\mathbf{u}^I(\mathbf{x})$  and  $\mathbf{t}^I(\mathbf{x})$ . It is then possible to use eq. (A3) again to calculate the displacements at any point  $\xi$  in  $D^I$  (Kawase 1988).

We now replace the material in the region  $D^E$ , exterior to  $D^I$ , by one that has the same stiffnesses and density as in  $D^I$ , and in which there are no sources. In doing so we shift the influence of the material in  $D^E$  to the boundary  $S$ . By taking the limit as  $\xi$  approaches  $S$  from outside  $D^I$  we can write a similar representation for the displacement in the exterior region:

$$a^E \tilde{u}_j(\xi) = -P \int_S [G_{ij}^I(\mathbf{x}, \xi) \tilde{t}_i(\mathbf{x}) - \tilde{u}_i(\mathbf{x}) T_{ij}^I(\mathbf{x}, \xi)] ds_x, \quad (\text{A4})$$

$$a^E = \begin{cases} 0 & \xi \text{ in } D^I, \\ 1 & \xi \text{ not in } D^I, \\ 0.5 & \xi \text{ on } S. \end{cases}$$

The body-force integral is dropped as it is zero. There is a change in sign in the integral over  $S$  since the sense of the outward normal to  $S$  is reversed. We use the same Green's function,  $G^I$ , as for the interior region since the material is the same. This must therefore satisfy the radiation conditions for outgoing waves. The limiting values  $\tilde{\mathbf{u}}$  and  $\tilde{\mathbf{t}}$  of the displacements and tractions are unspecified as yet. We can sum eqs (A3) and (A4) to obtain a representation for the displacement at any point  $\xi$  on  $S$ :

$$\frac{1}{2} [u_j^I(\xi) + \tilde{u}_j(\xi)] = P \int_S \{G_{ij}^I(\mathbf{x}, \xi) [t_i^I(\mathbf{x}) - \tilde{t}_i(\mathbf{x})] - T_{ij}^I(\mathbf{x}, \xi) [u_i^I(\mathbf{x}) - \tilde{u}_i(\mathbf{x})]\} ds_x + \iint_{D^I} f_i^I(\mathbf{y}) G_{ij}^I(\mathbf{y}, \xi) dA_y. \quad (\text{A5})$$

We specify the solution outside  $D^I$  to be that which establishes on  $S$  exactly the same boundary displacements as those in the initial interior-region problem [so that  $\tilde{\mathbf{u}}(\xi) = \mathbf{u}^I(\xi)$ ,  $\xi \in S$ ]. It follows that, in general,  $\mathbf{t}^I(\xi) \neq \mathbf{t}^E(\xi)$ . We now substitute  $\mathbf{u}^I(\xi)$

for  $\tilde{\mathbf{u}}(\xi)$  in eq. (A5) to obtain

$$u_j^I(\xi) = \int_S G_{ij}^I(\mathbf{x}, \xi) [t_i^I(\mathbf{x}) - \tilde{t}_i(\mathbf{x})] ds_x + \iint_{D^I} f_i^I(\mathbf{y}) G_{ij}^I(\mathbf{y}, \xi) dA_y. \quad (\text{A6})$$

With the notation  $\phi^I(\mathbf{x}) = \mathbf{t}^I(\mathbf{x}) - \tilde{\mathbf{t}}(\mathbf{x})$ , we can rewrite eq. (A6) as

$$u_j^I(\xi) = \int_S G_{ij}^I(\mathbf{x}, \xi) \phi_i^I(\mathbf{x}) ds_x + \iint_{D^I} f_i^I(\mathbf{y}) G_{ij}^I(\mathbf{y}, \xi) dA_y, \quad (\text{A7})$$

which shows that  $\phi^I(\mathbf{x}) ds_x$  represents a fictitious line-force distribution. Due to symmetry in the displacement Green's function [ $G_{ij}(\mathbf{x}, \xi) = G_{ji}(\xi, \mathbf{x})$ ] we can restate eq. (A7) as:

$$u_i^I(\mathbf{x}) = \int_S G_{ij}^I(\mathbf{x}, \xi) \phi_j^I(\xi) ds_\xi + \iint_{D^I} f_j^I(\xi) G_{ij}^I(\mathbf{x}, \xi) dA_\xi. \quad (\text{A8})$$

This integral representation (without the last term) is known as a single-layer potential and is classified as indirect because the scattered wavefield is given in terms of unknown source strengths located on the boundary. It is a mathematical expression of Huygen's principle, whereby every point on the boundary can be considered as a source of secondary wavelets. We have shown above the formal equivalence of the direct (eq. A3) and indirect (eq. A8) BEMs. Note that we could equally have chosen the solution outside  $S$  as that which establishes on  $S$  that  $\mathbf{t}^E(\xi) = \mathbf{t}^I(\xi)$ .

By application of Hooke's law to both sides of eq. (A8), an indirect representation of the interior tractions can be stated:

$$t_i^I(\mathbf{x}) = \frac{1}{2} \phi_i^I(\mathbf{x}) + P \int_S T_{ij}^I(\mathbf{x}, \xi) \phi_j^I(\xi) ds_\xi + c_{ipkl} \hat{n}_p \frac{\partial}{\partial x_l} P \iint_{D^I} f_j^I(\xi) G_{kj}^I(\mathbf{x}, \xi) dA_\xi, \quad (\text{A9})$$

where the first term on the right-hand side is a 'free term' due to the singularity when  $\mathbf{x}$  coincides with  $\xi$  on  $S$ , which is assumed to be smooth (Appendix C). The second term must again be treated as a Cauchy Principal Value.

The combination of eqs (A3) and (A4) also gives the displacement at any point  $\mathbf{x}$  within  $D^I$ :

$$u_i^{(r)}(\mathbf{x}) = \int_S G_{ij}^I(\mathbf{x}, \xi) \phi_j^I(\xi) ds_\xi + \iint_{D^I} f_j^I(\xi) G_{ij}^I(\mathbf{x}, \xi) dA_\xi. \quad (\text{A10})$$

In a similar way, the diffracted (outgoing) displacements  $\mathbf{u}^{(d)}$  in the exterior region  $D^E$  can be represented in terms of unknown source functions  $\phi^E$ :

$$u_i^{(d)}(\mathbf{x}) = \int_S G_{ij}^E(\mathbf{x}, \xi) \phi_j^E(\xi) ds_\xi + \iint_{D^E} f_j^E(\xi) G_{ij}^E(\mathbf{x}, \xi) dA_\xi, \quad (\text{A11})$$

where  $G_{ij}^E$  is the appropriate Green's function for the material in  $D^E$ . The limiting values  $\tilde{\mathbf{u}}^E$  and  $\tilde{\mathbf{t}}^E$  of the displacements  $\mathbf{u}^{(r)}$  and corresponding tractions  $\mathbf{t}^{(r)}$  on  $S$  are given by

$$u_i^E(\mathbf{x}) = \int_S G_{ij}^E(\mathbf{x}, \xi) \phi_j^E(\xi) ds_\xi + \iint_{D^E} f_j^E(\xi) G_{ij}^E(\mathbf{x}, \xi) dA_\xi, \quad (\text{A12})$$

$$t_i^E(\mathbf{x}) = -\frac{1}{2} \phi_i^E(\mathbf{x}) + P \int_S T_{ij}^E(\mathbf{x}, \xi) \phi_j^E(\xi) ds_\xi + c_{ipqk} \hat{n}_k \frac{\partial}{\partial x_q} \iint_{D^E} f_j^E(\xi) G_{pj}^E(\mathbf{x}, \xi) dA_\xi.$$

The unknown functions  $\phi^E$  and  $\phi^I$  are determined by matching the displacements and tractions on  $S$  due to, on the one hand, a combination of the interior refracted field  $\mathbf{u}^{(r)}$  and the exterior diffracted field  $\mathbf{u}^{(d)}$ , and on the other hand, the incident radiation  $\mathbf{u}^{(i)}$ :

$$\begin{aligned} u_j^E(\mathbf{x}) - u_j^I(\mathbf{x}) &= -u_j^{(i)}(\mathbf{x}), \\ t_j^E(\mathbf{x}) - t_j^I(\mathbf{x}) &= -t_j^{(i)}(\mathbf{x}), \quad \mathbf{x} \in S. \end{aligned} \quad (\text{A13})$$

### Fluid medium

A similar procedure can be used to derive direct and indirect representations for wave motion in a fluid medium (Dong 1993). The direct representation for the interior displacement potential  $\psi$  at a point  $\xi$  is, in the absence of sources,

$$a^I \psi^{(r)}(\xi) = P \int_S \hat{n}_i(\mathbf{x}) \left[ G^I(\mathbf{x}, \xi) \frac{\partial \psi^I(\mathbf{x})}{\partial x_j} - \psi^I(\mathbf{x}) \frac{\partial G^I(\mathbf{x}, \xi)}{\partial x_j} \right]_i ds_{\mathbf{x}}, \quad (\text{A14})$$

$$a^I = \begin{cases} 1 & \xi \text{ in } D^I, \\ 0 & \xi \text{ not in } D^I, \\ 0.5 & \xi \text{ on } S, \end{cases}$$

where  $\hat{\mathbf{n}}(\mathbf{x})$  is the outward-pointing unit normal at  $\mathbf{x}$  and  $G^I$  is the scalar potential Green's function for a fluid medium (Appendix B). The corresponding indirect expression is

$$\psi^{(r)}(\mathbf{x}) = \int_S G^I(\mathbf{x}, \xi) \phi^I(\xi) ds_{\xi}, \quad (\text{A15})$$

where  $\phi^I(\xi)$  is a distribution of fictitious sources. The indirect integral for the normal displacement  $u = \nabla \psi \cdot \hat{\mathbf{n}}$  at a point  $\mathbf{x}$  on the boundary  $S$  is

$$u^I(\mathbf{x}) = \frac{1}{2} \phi^I(\xi) + P \int_S T^I(\mathbf{x}, \xi) \phi^I(\xi) ds_{\xi}, \quad (\text{A16})$$

in which  $T^I$  is the normal displacement Green's function for a fluid medium:

$$T^I(\mathbf{x}, \xi) = \hat{n}_i(\mathbf{x}) \frac{\partial G^I(\mathbf{x}, \xi)}{\partial x_i}. \quad (\text{A17})$$

The pressure in the fluid is given by  $p^{(r)} = \rho \omega^2 \psi^{(r)}$ , where  $\rho$  is the fluid density, so the normal traction at the boundary is

$$\begin{aligned} t^I(\mathbf{x}) &= -p^I(\mathbf{x}) \\ &= -\rho \omega^2 \int_S G^I(\mathbf{x}, \xi) \phi^I(\xi) ds_{\xi}, \quad \mathbf{x} \in S. \end{aligned} \quad (\text{A18})$$

If the exterior region is solid, the conditions determining  $\phi^I$  and  $\phi^E$  are

$$\begin{aligned} u_j^E(\mathbf{x}) \hat{n}_j(\mathbf{x}) - u^I(\mathbf{x}) &= -u_j^{(i)}(\mathbf{x}) \hat{n}_j(\mathbf{x}), \\ t_j^E(\mathbf{x}) \hat{n}_j(\mathbf{x}) - t^I(\mathbf{x}) &= -t_j^{(i)}(\mathbf{x}) \hat{n}_j(\mathbf{x}), \\ t_j^E(\mathbf{x}) \hat{m}_j(\mathbf{x}) &= -t_j^{(i)}(\mathbf{x}) \hat{m}_j(\mathbf{x}), \end{aligned} \quad (\text{A19})$$

where  $\hat{\mathbf{m}}$  is a unit tangent to  $S$  at  $\mathbf{x}$ .

## APPENDIX B: GREEN'S FUNCTIONS FOR 2-D ISOTROPIC MEDIA

### Elastic medium

The Green's function for  $SH$  motion is given by

$$G(\mathbf{x}, \xi) = \frac{1}{4\mu i} H_0^{(2)}(k_{\beta} r), \quad r = |\mathbf{x} - \xi|, \quad (\text{B1})$$

where  $k_{\beta} = \omega / \beta$ , and  $\beta$  and  $\mu$  are respectively the  $S$ -wave speed and the modulus of rigidity in the material. This represents the displacement at  $\mathbf{x}$  due to an anti-plane unit force at  $\xi$ .

For steady-state  $P$ - $SV$  motion, the Green's function describes the displacement at  $\mathbf{x}$  in the  $i$ th direction as a result of the application of an in-plane unit force in the  $j$ th direction at  $\xi$ :

$$\begin{aligned} G_{ij}(\mathbf{x}, \xi) &= \frac{i}{4\mu} \left\{ \delta_{ij} H_0^{(2)}(k_{\beta} r) - \frac{1}{k_{\beta} r} \frac{\partial r}{\partial x_i} \frac{\partial r}{\partial x_j} \right. \\ &\quad \times \left[ H_1^{(2)}(k_{\beta} r) - \frac{\beta}{\alpha} H_1^{(2)}(k_{\alpha} r) \right] \left. \right\} \\ &\quad - \frac{i}{4\mu} \left\{ \frac{\partial r}{\partial x_i} \frac{\partial r}{\partial x_j} \left[ H_0^{(2)}(k_{\beta} r) - \frac{\beta^2}{\alpha^2} H_0^{(2)}(k_{\alpha} r) \right] \right\}, \end{aligned} \quad (\text{B2})$$

$$r = |\mathbf{x} - \xi|,$$

where  $k_{\alpha} = \omega / \alpha$  and  $\alpha$  is the  $P$ -wave speed.

### Fluid medium

The displacement potential Green's function in a fluid takes a similar form to the displacement for  $SH$  in an elastic medium:

$$G(\mathbf{x}, \xi) = \frac{1}{4i} H_0^{(2)}(k_f r), \quad (\text{B3})$$

where  $k_f$ , the wavenumber inside the fluid, is given by  $\omega / c$ , and  $c$  is the wave speed in the fluid.

The Green's functions given above can be found in Domínguez & Abascal (1984).

## APPENDIX C: EVALUATION OF THE BOUNDARY INTEGRALS

Expressions such as eq. (A2) for the displacement  $u^{(r)}(\xi)$  within the region  $D^I$ , that involve integrals like

$$\begin{aligned} &\int_S G_{ij}(\mathbf{x}, \xi) \Psi_i(\mathbf{x}) ds_{\mathbf{x}} \\ &\text{and} \\ &\int_S T_{ij}(\mathbf{x}, \xi) \psi_i(\mathbf{x}) ds_{\mathbf{x}} \end{aligned} \quad (\text{C1})$$

are not simple to evaluate in the limit as  $\xi$  approaches the boundary  $S$  since both  $G_{ij}$  and  $T_{ij}$  are singular at  $\xi = \mathbf{x}$ . We assume that the boundary is smooth and that  $\Psi$  and  $\psi$  represent continuous functions.

The Green's function  $G_{ij}$  in plane strain ( $P$ - $SV$  motion) is given by eq. (B2) and is a function of  $k_{\alpha} r$  and  $k_{\beta} r$ , where  $k_{\alpha} = \omega / \alpha$ ,  $k_{\beta} = \omega / \beta$  and  $r = |\mathbf{x} - \xi|$ . The limit  $r \rightarrow 0$  is, therefore, the same as the limit  $k_{\alpha} r \rightarrow 0$  and also  $\omega \rightarrow 0$ ; that is, the asymptotic behaviour for small  $r$  is the same as that for low

frequency, or the static limit. The 2-D static Green's function  $G_{ij}^s(\mathbf{x}, \xi)$  is given by Banerjee & Butterfield (1981) as

$$G_{ij}^s(\mathbf{x}, \xi) = \frac{-1}{8\pi\mu(1-\nu)} \{ (3-4\nu) \delta_{ij} \log r - \hat{r}_i \hat{r}_j \} + A_{ij}, \quad (\text{C2})$$

where  $\nu$  is Poisson's ratio,  $\hat{r}_i = (x_i - \xi_i)/r$  and  $A_{ij}$  is a constant tensor. There is therefore a logarithmic singularity in  $G_{ij}$  at  $\mathbf{x} = \xi$ , but this is integrable. The first of the integrals in eq. (C1) may therefore be evaluated in the limit as  $\xi \rightarrow \mathbf{x}^S \in S$  by simply setting  $\xi = \mathbf{x}^S$  in the integrand and evaluating the improper integral.

The second of the integrals in (C1) involves  $T_{ij}(\mathbf{x}, \xi)$ , given by

$$T_{ij}(\mathbf{x}, \xi) = c_{ipkl} \hat{n}_p(\mathbf{x}) \frac{\partial}{\partial x_l} G_{kj}(\mathbf{x}, \xi), \quad (\text{C3})$$

where  $\hat{\mathbf{n}}(\mathbf{x})$  is the outward normal to the boundary  $S$ . The static equivalent of this is (Banerjee & Butterfield 1981)

$$T_{ij}^s(\mathbf{x}, \xi) = \frac{-1}{4\pi r(1-\nu)} \{ (1-2\nu)(\hat{n}_j \hat{r}_i - \hat{n}_i \hat{r}_j) + [(1-2\nu)\delta_{ij} + 2\hat{r}_i \hat{r}_j] \hat{r}_k \hat{n}_k \}, \quad (\text{C4})$$

and this has a  $(1/r)$  singularity that is not integrable when  $\xi = \mathbf{x}^S \in S$ . We therefore need to look carefully at the details of the limit as  $\xi \rightarrow \mathbf{x}^S$ , where  $\mathbf{x}^S$  is any point of  $S$ .

The derivation of the final result given by Banerjee & Butterfield (1981) is given only for the acoustic (scalar) case and is, in any case, not valid in all circumstances.

Consider the point  $\xi$  within the region  $D^I$  as it approaches a point  $\mathbf{x}^S$  on the boundary  $S$  of  $D^I$  (see Fig. C1). We split the curve  $S$  into two parts, namely  $S_\epsilon$ , a section of curve centred on  $\mathbf{x}^S$  and of length  $\epsilon$  on either side, and  $S' = S - S_\epsilon$ . The main task is to evaluate

$$\lim_{\xi \rightarrow \mathbf{x}^S} \int_{S_\epsilon} T_{ij}(\mathbf{x}, \xi) \psi_i(\mathbf{x}) ds_x. \quad (\text{C5})$$

To do this, we split the integral into two further parts:

$$\begin{aligned} \int_{S_\epsilon} T_{ij}(\mathbf{x}, \xi) \psi_i(\mathbf{x}) ds_x &= \psi_i(\mathbf{x}^S) \int_{S_\epsilon} T_{ij}(\mathbf{x}, \xi) ds_x \\ &+ \int_{S_\epsilon} T_{ij}(\mathbf{x}, \xi) [\psi_i(\mathbf{x}) - \psi_i(\mathbf{x}^S)] ds_x. \end{aligned} \quad (\text{C6})$$

If  $\psi$  is Hölder continuous on  $S$ ,

$$|\psi_i(\mathbf{x}_1) - \psi_i(\mathbf{x}_2)| \leq L |\mathbf{x}_1 - \mathbf{x}_2|^\alpha \quad (\text{C7})$$

for any two points  $\mathbf{x}_1, \mathbf{x}_2$  of  $S$ , where  $L$  and  $\alpha$  are constants, with  $0 < \alpha \leq 1$ . On the assumption that this inequality holds, the second integral in eq. (C6) is integrable and bounded when  $\xi = \mathbf{x}^S$ . It remains to evaluate the first of the integrals in (C6).

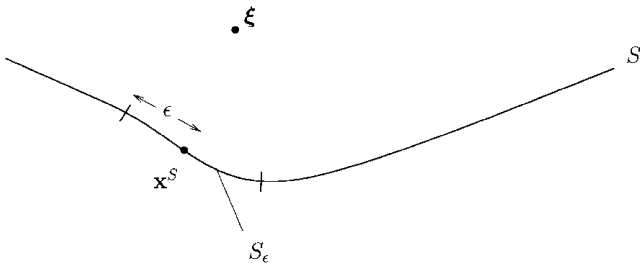


**Figure C1.** The boundary  $S$  is divided into two parts by taking out a section  $S_\epsilon$  of length  $2\epsilon$ , with the boundary point  $\mathbf{x}^S$  in the middle.

We have assumed that  $S$  is smooth and so we may replace the curve  $S_\epsilon$  by a section of straight line, tangent to  $S_\epsilon$  at  $\mathbf{x}^S$  (see Fig. C2) with error of the order of  $\epsilon$ :

$$\int_{S_\epsilon} T_{ij}(\mathbf{x}, \xi) ds_x = \int_{-\epsilon}^{\epsilon} T_{ij}(\mathbf{x}, \xi) dx + O(\epsilon), \quad (\text{C8})$$

where we have set up axes oriented such that  $\mathbf{x}^S$  lies at the origin, the  $x$ -axis lies along the tangent [so that  $\mathbf{x} = (x, 0)$ ,  $-\epsilon \leq x \leq \epsilon$ ] and the  $y$ -axis points into  $D^I$  so that  $\xi = (0, \eta)$ ,  $\hat{\mathbf{n}}(\mathbf{x}) = (0, -1)$ .

Since  $|\mathbf{x} - \xi|$  is arbitrarily small in this integral, we use the static form for  $T_{ij}$ . Substituting for  $\mathbf{x}, \xi$  and  $\hat{\mathbf{n}}$  in eq. (C4) we obtain

$$\begin{aligned} T_{11}(\mathbf{x}, \xi) &= \frac{-1}{4\pi r(1-\nu)} \frac{\eta}{r} \left\{ 1 - 2\nu + 2 \frac{x^2}{r^2} \right\}, \\ T_{12}(\mathbf{x}, \xi) &= \frac{-1}{4\pi r(1-\nu)} \left\{ -(1-2\nu) \frac{x}{r} - \frac{2\eta^2 x}{r^3} \right\}, \\ T_{21}(\mathbf{x}, \xi) &= \frac{-1}{4\pi r(1-\nu)} \left\{ (1-2\nu) \frac{x}{r} - \frac{2\eta^2 x}{r^3} \right\}, \\ T_{22}(\mathbf{x}, \xi) &= \frac{-1}{4\pi r(1-\nu)} \frac{\eta}{r} \left\{ 1 - 2\nu + 2 \frac{\eta^2}{r^2} \right\}, \end{aligned} \quad (\text{C9})$$

where  $r = (x^2 + \eta^2)^{1/2}$ . In the integration over  $x$ , odd powers of  $x$  give zero contribution, so that the integrals of  $T_{12}$  and  $T_{21}$  are both zero.

The remaining integrals are

$$\begin{aligned} \int_{-\epsilon}^{\epsilon} T_{11}(\mathbf{x}, \xi) dx &= \frac{-\eta}{4\pi(1-\nu)} \int_{-\epsilon}^{\epsilon} \left\{ \frac{1-2\nu}{x^2 + \eta^2} + \frac{2x^2}{(x^2 + \eta^2)^2} \right\} dx \\ &= \frac{-1}{4\pi(1-\nu)} \left\{ 4(1-\nu) \tan^{-1} \epsilon / \eta - \frac{2\epsilon\eta}{(\epsilon^2 + \eta^2)} \right\}, \\ \int_{-\epsilon}^{\epsilon} T_{22}(\mathbf{x}, \xi) dx &= \frac{-\eta}{4\pi(1-\nu)} \int_{-\epsilon}^{\epsilon} \left\{ \frac{1-2\nu}{x^2 + \eta^2} + \frac{2\eta^2}{(x^2 + \eta^2)^2} \right\} dx \\ &= \frac{-1}{4\pi(1-\nu)} \left\{ 4(1-\nu) \tan^{-1} \epsilon / \eta + \frac{2\epsilon\eta}{(\epsilon^2 + \eta^2)} \right\}. \end{aligned} \quad (\text{C10})$$

If we now let  $\xi \rightarrow \mathbf{x}^S$  ( $\eta \rightarrow 0$ ), we have

$$\int_{S_\epsilon} T_{ij}(\mathbf{x}, \xi) ds_x = \frac{-1}{2} \delta_{ij} + O(\epsilon). \quad (\text{C11})$$

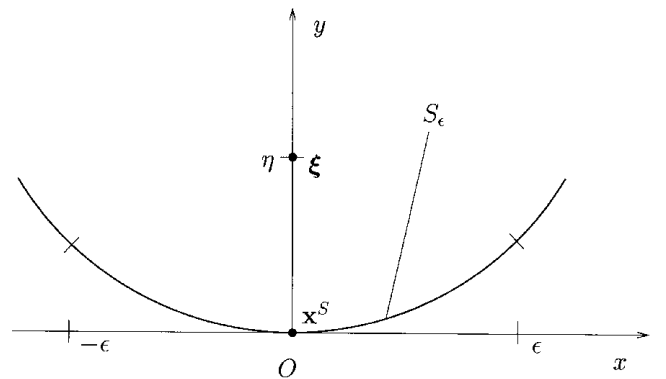


**Figure C2.** The section of boundary  $S_\epsilon$  is replaced by an interval  $[-\epsilon, \epsilon]$  on the tangent at the point  $\mathbf{x}^S$ .

Finally, we allow  $\epsilon$  to tend to zero. The integral over  $S'$  becomes a Cauchy Principal Value and the second integral on the right of eq. (C6) tends to zero. Thus

$$\lim_{\xi \rightarrow \mathbf{x}^S, \xi \in D^I} \int_S T_{ij}(\mathbf{x}, \xi) \psi_j(\mathbf{x}) ds_{\mathbf{x}} = P \int_S T_{ij}(\mathbf{x}, \mathbf{x}^S) \psi_j(\mathbf{x}) ds_{\mathbf{x}} - \frac{1}{2} \psi_j(\mathbf{x}^S). \quad (\text{C12})$$

If the point  $\xi$  lies outside  $D^I$ , we may repeat the derivation, changing the sign of  $\eta$  in eq. (C9). This leads to the same result except that the sign of the 'free term' is changed:

$$\lim_{\xi \rightarrow \mathbf{x}^S, \xi \notin D^I} \int_S T_{ij}(\mathbf{x}, \xi) \psi_j(\mathbf{x}) ds_{\mathbf{x}} = P \int_S T_{ij}(\mathbf{x}, \mathbf{x}^S) \psi_j(\mathbf{x}) ds_{\mathbf{x}} + \frac{1}{2} \psi_j(\mathbf{x}^S). \quad (\text{C13})$$

These results justify the step from eq. (A2) to eq. (A3).

The derivation of eq. (A9) from (A8) follows a slightly different path. Eq. (A8) shows the displacement within  $D^I$  represented in terms of a single-layer potential  $\phi$ ; that is, with the body force  $\mathbf{f}$  set to zero:

$$u_i(\mathbf{x}) = \int_S G_{ij}(\mathbf{x}, \xi) \phi_j(\xi) ds_{\xi}, \quad \mathbf{x} \in D^I. \quad (\text{C14})$$

The corresponding stress field is

$$\sigma_{ij}(\mathbf{x}) = \int_S c_{ijpq} G_{pk,q}(\mathbf{x}, \xi) \phi_k(\xi) ds_{\xi}, \quad \mathbf{x} \in D^I. \quad (\text{C15})$$

We need to evaluate the displacements and tractions on  $S$ . As before, the singularity in  $G_{ij}$  at  $\mathbf{x} = \xi$  is integrable and we may simply put  $\mathbf{x} = \mathbf{x}^S$  in eq. (C13). To find the tractions, we need to take the limit as  $\mathbf{x} \rightarrow \mathbf{x}^S$ :

$$t_i(\mathbf{x}^S) = \lim_{\mathbf{x} \rightarrow \mathbf{x}^S} \int_S c_{ijpq} \hat{n}_j(\mathbf{x}^S) G_{pk,q}(\mathbf{x}, \xi) \phi_k(\xi) ds_{\xi}. \quad (\text{C16})$$

This is similar to taking the limit as  $\xi \rightarrow \mathbf{x}^S$  of the second integral in (C1) except that  $\hat{\mathbf{n}}(\mathbf{x})$  is replaced by  $\hat{\mathbf{n}}(\mathbf{x}^S)$  and the integration is over  $\xi$  instead of  $\mathbf{x}$ . We may in fact write

$$t_i(\mathbf{x}^S) = \lim_{\mathbf{x} \rightarrow \mathbf{x}^S} \int_S F_{ij}(\mathbf{x}, \xi) \phi_j(\xi) ds_{\xi}, \quad (\text{C17})$$

where

$$F_{ij}(\mathbf{x}, \xi) = c_{ipkl} \hat{n}_p(\mathbf{x}^S) \frac{\partial}{\partial x_l} G_{kj}(\mathbf{x}, \xi). \quad (\text{C18})$$

We proceed as before to evaluate the integral in (C17) by dividing the range of integration into a part over  $S_{\epsilon}$  and a part over  $S' = S - S_{\epsilon}$ . The integral over  $S'$  will become a Cauchy Principal Value when  $\epsilon \rightarrow 0$ ; the integral over  $S_{\epsilon}$  is partitioned as in eq. (C6):

$$\begin{aligned} \int_{S_{\epsilon}} F_{ij}(\mathbf{x}, \xi) \phi_j(\xi) ds_{\xi} &= \phi_j(\mathbf{x}^S) \int_{S_{\epsilon}} F_{ij}(\mathbf{x}, \xi) ds_{\xi} \\ &+ \int_{S_{\epsilon}} F_{ij}(\mathbf{x}, \xi) [\phi_j(\xi) - \phi_j(\mathbf{x}^S)] ds_{\xi}. \end{aligned} \quad (\text{C19})$$

The second integral is bounded as  $\mathbf{x} \rightarrow \mathbf{x}^S$  and tends to zero as  $\epsilon \rightarrow 0$ . It remains, therefore, to evaluate the first integral and take the limit as  $\mathbf{x} \rightarrow \mathbf{x}^S$ . This proceeds exactly as for the integral over  $T_{ij}$  in (C8) except that  $\mathbf{x}$  and  $\xi$  have been interchanged. Since  $T_{ij}$  (and therefore  $F_{ij}$ ) is an odd function of  $\hat{\mathbf{r}} = (\mathbf{x} - \xi)/r$ ,

the result is as before but with the opposite sign:

$$\int_{S_{\epsilon}} F_{ij}(\mathbf{x}, \xi) ds_{\xi} = \frac{1}{2} \delta_{ij} + O(\epsilon). \quad (\text{C20})$$

We now let  $\epsilon \rightarrow 0$  to obtain

$$t_i(\mathbf{x}^S) = P \int_S T_{ij}(\mathbf{x}^S, \xi) \phi_j(\xi) ds_{\xi} + \frac{1}{2} \phi_i(\mathbf{x}^S), \quad (\text{C21})$$

which leads to eq. (A9).

The derivation of eq. (A12) proceeds in exactly the same way except that the limit is approached from outside  $D^I$  and so the sign of the free term is changed.

The corresponding expressions for the anti-plane-strain (SH) problem involve integrals such as

$$\int_S G(\mathbf{x}, \xi) \Psi(\mathbf{x}) ds_{\mathbf{x}} \quad \text{and} \quad \int_S T(\mathbf{x}, \xi) \psi(\mathbf{x}) ds_{\mathbf{x}}, \quad (\text{C22})$$

where the Green's function is now (eq. B1)

$$G(\mathbf{x}, \xi) = \frac{1}{4\mu i} H_0^{(2)}(k_{\beta} r) \quad (\text{C23})$$

and

$$T(\mathbf{x}, \xi) = \mu \hat{n}_j(\mathbf{x}) \frac{\partial}{\partial x_j} G(\mathbf{x}, \xi) = \frac{-k_{\beta} \hat{n}_j(\mathbf{x}) \hat{r}_j}{4i} H_1^{(2)}(k_{\beta} r); \quad (\text{C24})$$

$\hat{\mathbf{n}}(\mathbf{x})$  is once again the unit outward normal on  $S$ .

The leading terms for the Hankel functions of small argument are (Ryshik & Gradstein 1963)

$$\begin{aligned} H_0^{(2)}(z) &= \frac{-2i}{\pi} \log z + O(1), \\ H_1^{(2)}(z) &= \frac{2i}{\pi z} + O(1). \end{aligned} \quad (\text{C25})$$

It follows, as for the plane-strain case, that the first integral in (C22) may be evaluated directly for  $\xi = \mathbf{x}^S \in S$ , whereas we need to take the limit  $\xi \rightarrow \mathbf{x}^S$  to evaluate the second.

We proceed, as before, to write

$$\int_S T(\mathbf{x}, \xi) \psi(\mathbf{x}) ds_{\mathbf{x}} = \int_{S'} T(\mathbf{x}, \xi) \psi(\mathbf{x}) ds_{\mathbf{x}} + \int_{S_{\epsilon}} T(\mathbf{x}, \xi) \psi(\mathbf{x}) ds_{\mathbf{x}}. \quad (\text{C26})$$

The first integral takes the Cauchy Principal Value when  $\mathbf{x} = \mathbf{x}^S$  and  $\epsilon \rightarrow 0$ . The second integral becomes

$$\begin{aligned} \int_{S_{\epsilon}} T(\mathbf{x}, \xi) \psi(\mathbf{x}) ds_{\mathbf{x}} &= \psi(\mathbf{x}^S) \int_{S_{\epsilon}} T(\mathbf{x}, \xi) ds_{\mathbf{x}} \\ &+ \int_{S_{\epsilon}} T(\mathbf{x}, \xi) [\psi(\mathbf{x}) - \psi(\mathbf{x}^S)] ds_{\mathbf{x}}. \end{aligned} \quad (\text{C27})$$

The second integral here is bounded as  $\mathbf{x} \rightarrow \mathbf{x}^S$  (assuming Hölder continuity for  $\psi$ ) and tends to zero as  $\epsilon \rightarrow 0$ . The first becomes

$$\int_{S_{\epsilon}} T(\mathbf{x}, \xi) ds_{\mathbf{x}} = \int_{-\epsilon}^{\epsilon} T(\mathbf{x}, \xi) d\mathbf{x} + O(\epsilon) \quad (\text{C28})$$

by the replacement of  $S_{\epsilon}$  by a section of the tangent at  $\mathbf{x}^S$  (see Fig. C2).

We choose axes so that  $\mathbf{x}^S = (0, 0)$ ,  $\xi = (0, \eta)$ ,  $\mathbf{x} = (x, 0)$  and  $\hat{\mathbf{n}} = (0, -1)$ ; thus,

$$T(\mathbf{x}, \xi) = \frac{-\eta}{2\pi r^2} + O(1), \quad (\text{C29})$$

where  $r^2 = x^2 + \eta^2$ . Substituting back into (C28) and performing the integration, we obtain

$$\int_{S_\epsilon} T(\mathbf{x}, \xi) ds_{\mathbf{x}} = -\frac{1}{\pi} \tan^{-1}(\epsilon/\eta) + O(\epsilon). \quad (\text{C30})$$

Finally we take the limits  $\eta \rightarrow 0$  and then  $\epsilon \rightarrow 0$  to obtain

$$\lim_{\xi \rightarrow \mathbf{x}^S} \int_S T(\mathbf{x}, \xi) \psi(\mathbf{x}) ds_{\mathbf{x}} = P \int_S T(\mathbf{x}^S, \xi) \psi(\mathbf{x}) ds_{\mathbf{x}} - \frac{1}{2} \psi(\mathbf{x}^S). \quad (\text{C31})$$

This establishes the formula in anti-plane strain for points  $\xi$  on  $S$ .

Exactly the same procedure can be followed to establish eqs (A9) and (A12) and the signs of the free terms for anti-plane strain.

For a fluid medium, the expressions that need to be evaluated are the same as in eq. (C22) but with (eq. B3)

$$G(\mathbf{x}, \xi) = \frac{1}{4i} H_0^{(2)}(k_f r) \quad (\text{C32})$$

and

$$T(\mathbf{x}, \xi) = \hat{n}_j(\mathbf{x}) \frac{\partial}{\partial x_j} G(\mathbf{x}, \xi) = \frac{-k_f \hat{n}_j(\mathbf{x}) \hat{r}_j}{4i} H_1^{(2)}(k_f r), \quad (\text{C33})$$

where  $k_f$  is the wavenumber in the fluid. Thus  $T$  is exactly the same as for anti-plane-strain ( $SH$ ) motion in a solid and the limit of the integral as  $\mathbf{x} \rightarrow \mathbf{x}^S \in S$  is the same. This establishes (A14) and (A16).